EES Solar

PAPER

View Article Online
View Journal | View Issue

Cite this: *EES Sol.*, 2026, **2**, 183

In-depth investigation of methylamine gas post-treatment for $MAPbI_3$ films and its potential for upscaling perovskite solar cells

Duc-Anh Le [a] and Tzu-Chien Wei *[ab]

Scaling up perovskite solar cells (PSCs) for commercial applications requires maintaining film quality across large areas, a challenge often compounded by morphological defects and chemical heterogeneity. Methylamine gas treatment (MATM) offers a promising post-processing strategy by inducing liquefaction and recrystallization of methylammonium-based perovskite films, thereby enhancing their uniformity and chemical homogeneity. However, how to properly conduct the MATM, particularly the influence of environmental humidity on its outcome, has rarely been investigated. In this study, we report that environmental moisture critically undermines MATM efficacy by triggering side reactions that generate PbO, PbIOH, and $MAPbI_2OH$ impurities. Through systematic comparison of $MAPbI_3$ films treated under dry and humid conditions, we elucidate the degradation mechanisms using various analyses and conclude moisture exposure during MATM drastically increases trap densities and non-radiative recombination, leading to reduced carrier lifetimes and photovoltaic performance. A PSC with an initial power conversion efficiency (PCE) of 16.67% exhibits a significant improvement to 19.48% after undergoing MATM in a dry environment. In contrast, when MATM is performed under humid conditions, although the surface smoothness of the $MAPbI_3$ film is greatly improved, the PCE of the device declines instead of increasing. This outcome highlights the detrimental effects of side reactions induced by moisture during the MATM process. These findings underscore the importance of moisture isolation in MATM to enable the reliable upscaling of high-efficiency and stable perovskite solar modules.

Received 5th September 2025
Accepted 3rd November 2025

DOI: 10.1039/d5el00143a

rsc.li/EESSolar

Broader context

Scaling up perovskite solar cells (PSCs) for commercial applications requires maintaining high film quality over large areas, a challenge hindered by morphological defects and chemical inconsistencies. Most existing approaches to large-area fabrication involve modifying the drying process – such as using co-solvents or alternative techniques – to improve film uniformity. While these methods enhance film quality compared to small-area antisolvent processes, they still result in performance losses during scale-up, indicating that a truly lossless transition to large-area devices has not yet been achieved. We propose that a more practical and effective solution lies in post-treatment strategies that repair or modify films after deposition to homogenize morphology and composition. Among these, methylamine gas treatment (MATM), which induces film liquefaction and recrystallization, shows particular promise. This method offers the potential to enhance film uniformity and preserve device efficiency during scaling. In our earlier research, we demonstrated control of MATM through adsorption kinetics and developed a prototype reactor capable of uniformly treating substrates as large as 10 cm × 10 cm, laying the groundwork for scalable, efficiency-retaining fabrication of perovskite films.

Introduction

Organic lead halide perovskites (PVSKs) have garnered significant attention in recent years as absorbers for photovoltaic devices due to their low exciton binding energy, high extinction coefficient and exceptional defect tolerance.[1–5] Since Miyasaka's group first reported perovskite solar cells (PSCs) based on these materials in 2009, their power conversion efficiency (PCE) has sharply increased to 27.0%, rivalling that of crystalline silicon photovoltaic technology, which has been developed for over half a century.[6,7] Despite this impressive progress, such high PCE PSCs were achieved primarily on very small active areas (mostly <0.1 cm^2). However, in practical applications, the performance of photovoltaic devices is evaluated by the power output rather than efficiency alone. Thus, the ability to maintain a high PCE over large-area substrates has become a critical challenge in the commercialization of PSCs.

An ideal PVSK layer should exhibit a homogeneous chemical composition, a compact and smooth morphology, and low impurity content. After more than a decade of effort, these

[a]*Department of Chemical Engineering, National Tsing Hua University, 101, Sec. 2, Guang-Fu Road, Hsinchu, Taiwan 30013, Republic of China. E-mail: tcwei@mx.nthu.edu.tw*

[b]*Research Center for Critical Issues, Academia Sinica, Tainan, Taiwan, Republic of China*

properties can now be reliably achieved in small-area devices. Despite the promising results achieved with small-area devices, the application of these techniques to large-area substrates remains technically challenging, particularly in terms of uniform film formation, defect control, and process reproducibility. Various methods for fabricating large-area perovskite absorber layers have been reported, among which solution-based, wet-coating processes remain the most mature and widely applied. These approaches involve dissolving perovskite precursors in highly polar organic solvents, coating them onto substrates to form wet films, and then inducing crystallization by removing the solvent. Based on a literature survey on large-area PVSK thin film fabrication, the process can be generally divided into three steps:

Step-1: Deposition of the wet precursor film, using methods such as spin coating,[8] slot-die coating,[9] spray coating,[10,11] screen printing,[12] and inkjet printing.[13]

Step-2: Drying and crystallization to form a primary PVSK film, using techniques such as anti-solvent treatment,[14,15] thermal annealing,[16] vacuum-assisted drying,[17,18] or hot wind drying.[19,20]

Step-3: Post-treatment to further improve PVSK film quality, such as passivation, solvent annealing[21–23] or liquefaction–recrystallization strategies.[24,25]

It is worth noting that in many reports on large-area PSCs, the precursor solution used in Step-1 is often supplemented with a secondary solvent or specific additives to modulate the crystallization behaviour and improve the morphology and quality of the resulting PVSK films[26–29] Among these three steps, we believe that Step-3, the post-treatment stage, is particularly critical for future large-scale production, as it possibly provides a "healing" mechanism to fix the quality of the primary PVSK film formed in Step-2, if it is properly designed. This, in turn, reduces the precision demands and investment on both the coating equipment and the solvent removal systems, which can have a positive impact on lowering manufacturing costs and improving production yield.

The liquefaction–recrystallization strategy is one typical example of Step-3, and it involves reacting the primary PVSK film (formed after Step-2) with amine compounds to produce a chemically adsorbed intermediate in a liquid phase. This liquid intermediate allows for self-levelling of the film, and upon removal of the amine species, a recrystallized PVSK film (hereafter named as secondary PVSK) with enhanced uniformity and compactness can be obtained. A representative showcase of this strategy is the methylamine gas treatment (MATM) for MA-based perovskites. Methylamine (MA^0) is a volatile chemical (boiling point −6 °C) that can rapidly react with $MAPbI_3$, inducing liquefaction of the perovskite layer within less than one second. Subsequent removal of MA^0 leads to recrystallization, enhancing crystal quality and reducing defect density, thereby improving PSC performance.[24,25,30–33]

MATM was first proposed by Pang *et al.* in 2015, who attributed the liquefaction–recrystallization mechanism to interactions between the lone electron pair on the nitrogen atom of MA^0 and the PbI_6 octahedra in $MAPbI_3$, disrupting the 3D crystal structure and resulting in liquefaction. Other studies have shown that PbI_2, a common precursor in perovskite formation, can also transit into a molten state upon exposure to MA^0 or other amines, suggesting that the liquefaction is driven by coordination between Pb^{2+} ions and amines.[24,25,30,34–37] Kerner *et al.* further reported that the formation of Pb–amide bonds *via* proton transfer plays a critical role in triggering the liquefaction.[38]

As noted above, the adsorption and desorption kinetics in MATM are extremely rapid, with the liquefaction occurring within ~1 second.[32] This narrow process window poses a major challenge for implementing MATM in scalable manufacturing systems. To address this issue, we have developed a controllable MATM technique in which the partial pressure of MA^0 is finely tuned to control the liquefaction kinetics. We have found that the amount of MA^0 adsorbed onto the primary $MAPbI_3$ film significantly influences the morphology and crystallinity of the resulting secondary film. Moderately reducing the MA^0 concentration during MATM facilitates the formation of high-quality films. Using our home-made MATM chamber, we successfully scaled up the process from small-area devices to 5 cm × 5 cm mini-modules without PCE loss.[31]

To further evaluate the industrial feasibility of MATM, this study investigates the influence of environmental moisture during treatment, as humidity content is an important factor in PSC fabrication. In 2020, Bogachuk *et al.* reported that MA^0 reacted with $MAPbI_3$ powders in humid environments to form photo-inactive by-products such as PbIOH, demonstrating that moisture can significantly hinder successful recrystallization during MATM.[39] Controlling humidity during production is closely tied to manufacturing cost. Therefore, humidity not only affects the outcome of MATM but also represents a critical consideration in the design of future PSC production lines. Based on this background, this study systematically examines the effect of ambient humidity on the crystallinity, morphology, and optoelectronic properties of secondary $MAPbI_3$ films treated with MA^0. We further correlate these findings with device performance, stability, and reproducibility, in order to strengthen the feasibility of this method for future large-scale PSC manufacturing.

Experimental section

Substrate cleaning

Fluorine doped tin oxide glass (FTO, 2.2 mm thick, 8 Ω sq.$^{-1}$, Dyesol) was dry etched with a laser machine (LMF-020F, Laser Life Company, Taiwan). The etched FTO was cleaned with detergent solution (PK-LCG46, Parker International Co. Ltd, Taiwan) and by reverse osmosis (RO), then rinsed with deionized water (DI) and ethanol 95% (ECHO, Taiwan), and dried with a hot-air blow gun. Before compact layer TiO_2 ($cTiO_2$) deposition, the cleaned FTO substrate was treated by UV/ozone for 30 min.

Electron transport layer (ETL)

The $cTiO_2$ precursor solution was prepared by mixing 6% v/v of titanium diisopropoxide bis(acetylacetonate) solution, 4% v/v of

acetylacetonate and ethanol. The $cTiO_2$ precursor was sprayed on hot reheated FTO for 8 circles. The flow of O_2 was controlled at 0.4 L min^{-1}, and 1 min resting time was used for each circle. After the spraying process, the substrates were annealed at 500 °C for 30 min.

A commercial paste TiO_2 (30 NR-D, GreatcellSolar) was diluted in ethanol absolute 99.8% (Honeywell) with ratio 1 : 7 (weight). Then, it was coated onto the $cTiO_2$ substrate at 6000 rpm for 30 s. The mesoporous TiO_2 ($msTiO_2$) coated substrate was dried on the 120 °C hotplate for 5 min, then the $msTiO_2$ films were gradually heated to 500 °C and cooled to room temperature. After cooling down to 150 °C, the $msTiO_2$ substrate was treated by UV-ozone for 20 min, and then transferred to a humidity-controlled room (10–20% humidity) for the preparation of perovskite films.

PVSK fabrication

A PVSK precursor solution contains 1.5 M PbI_2 (99.0%, Xian Polymer Chemicals) 1.5 M MAI (GreatcellSolar) and 0.35 M MACl (99.9%, GreatcellSolar) in DMF : DMSO (99.9%, Sigma-Aldrich) mix solvent (volume ratio = 9 : 1). **Primary-$MAPbI_3$** films were prepared by coating the precursor solution onto the $msTiO_2$ substrate at 3000 rpm for 10 s, and then the wet PVSK film was transferred to a vacuum chamber with continuous N_2 flow. The pressure of the chamber was controlled at 150 torr, and the PVSK film was in vacuum for 30 seconds. After that, the dried PVSK film was heated at 150 °C for 10 min.

MATM under various moisture conditions

A MA^0 induced liquefaction and recrystallization reactor (MALCR) was used to prepare MA^0-treated $MAPbI_3$ films (**2nd-$MAPbI_3$/dry**). MA^0 gas was generated from a 33 wt% MA^0 ethanol solution (Sigma-Aldrich). The effective MA^0 concentration was determined using Raoult's law, and the measured vapor pressure (149 kPa) corresponded to ~45% MA^0 concentration during MATM. The **Primary-$MAPbI_3$** films were moved into the MALCR system and vacuum for 5 min to remove moisture absorption on PVSK films. Then, MA^0 gas was exposed into the reaction chamber. At the point during exposure where the PVSK completely changes to transparent (a few seconds), the MALCR chamber was vacuumed to remove MA^0 gas. The transparent film changes back to the dark brown film. Then, the pressure was released and the **2nd-$MAPbI_3$/dry** films were moved onto the 100 °C hotplate for 10 min to completely remove remaining MA^0 gas on the PVSK films.

For the MATM in the presence of moisture, the MA^0 gas was premixed with air from a controlled dry room (25 °C, 20% RH) before injection into the MALCR. Thus, the chamber humidity was maintained consistently at 20% RH throughout the treatment for 5 minutes. **2nd-$MAPbI_3$/wet** films were then obtained after evacuating the chamber to complete the desorption process. **2nd-MAPbI3/wet/heat** films were prepared by heating the **2nd-MAPbI3/wet** films at 100 °C for 5 min.

After cooling down to room temperature, the **2nd-$MAPbI_3$** films were moved back to the humidity-control room to deposit the hole transporting material (HTM).

Hole transporting layer (HTL) deposition

The HTM precursor containing 32 mM lithium bis(trifluoromethanesulfonyl)imide (Li-TFSI, >99.9%, Sigma-Aldrich), and 195 mM 4-*tert*-butylpyridine (4-tBP, 96%, Sigma-Aldrich) in CB was left to stir at room temperature for 1 day. 2,2′,7,7′-Tetrakis[*N*,*N*-di(4-methoxyphenyl)amino]-9,9′-spirobifluorene (Spiro-OMeTAD, 99.5%, Lumtec) powder was added into the HTM precursor (75 mM) to form the HTM solution. The HTM solution was spin-coated onto the FTO/ETL/perovskite substrate at 4000 rpm for 25 s. Then, the pre-mature devices (FTO/ETL/PVSK/HTL) were stored in a dark and dry box (RH = 10%) overnight.

Electrode deposition

An ~100 nm thickness gold electrode was thermally evaporated onto the HTL at 1×10^{-6} mbar.

Module fabrication

The FTO glass was cut into 4 cm × 4 cm or 5 cm × 5 cm pieces, and then P1 was scribed by using a laser machine with a 532 nm laser (Lifelaser Co., Ltd). The laser speed, power ratio and frequency were 300 mm s^{-1}, 40% and 20 kHz, respectively. The etched FTO was cleaned by following the substrate cleaning process. Before spraying $cTiO_2$, the clean FTO was cleaned under UV-O_3 for 30 min then reheated at 500 °C for 30 min and kept at 500 °C during the spraying process.

$cTiO_2$ and $msTiO_2$ coatings were prepared following the methods used for the spray-coating compact layer and spin-coating mesoporous layer above. After annealing $msTiO_2$ and cooling down to 150 °C, the TiO_2 substrate was treated by UV-ozone for 30 min, then transferred to a humidity-controlled room (10–15% humidity) for the preparation of PVSK films. The PVSK precursor was prepared as above and denoted as 1.5 M $MAPbI_3$. The PVSK coating followed the coating process using the vacuum method.

The MATM was operated by using the home-made MALCR as the **2nd-$MAPbI_3$/dry** film preparation. The MA solution (33 wt% in absolute ethanol) was stored in a MA^0 source chamber. Another chamber was used as the reacting chamber. The reacting chamber was vacuum drawn to reach around 8 torr on the sensor. Then the valve, which connected the MA^0 source chamber and reacting chamber, was slowly opened until the pressure value on the sensor reached 150 Torr. N_2 flow and vacuum pump were used to purge MA^0 gas out of the MATM chamber. Then, PVSK films were heated at 100 °C for 10 min.

The pre-solution containing 16 mM Li-TFSI and 85 mM 4-tBP in CB was kept stirring at room temperature for 1 day. The Spiro-OMeTAD powder was added into the pre-solution (35.5 mM) as the HTM solution. The HTM solution was spin-coated onto the perovskite film at 2000 rpm for 25 s.

Then, the pre-mature devices (FTO/ETL/perovskite/HTL) were P2 scribed by using a laser with 100% power ratio, 70 kHz in frequency and 1800 mm s^{-1} speed of laser. Then, the pre-mature devices were stored in a dark and dry box (RH = 10%) overnight.

An ~100 nm thickness gold electrode was thermally evaporated onto the HTL at 1×10^{-6} mbar. Finally, P3 scribing was performed by using the same laser as that for P2 with a laser power ratio of 100%, frequency of 80 kHz and 1800 mm s^{-1}.

Characterization

The surface morphology of the samples was examined using field-emission scanning electron microscopy (FESEM, HITACHI, Japan), while atomic force microscopy (AFM, C3000 Nanosurf, Switzerland) was employed to assess surface roughness. The optical properties were characterized through ultraviolet-visible (UV-vis) spectroscopy using a spectrometer (UV-vis HP8453, USA). Steady-state and time-resolved photoluminescence (PL and TRPL) measurements were conducted with a photoluminescence spectrometer (FS5 EDINBURGH Instrument, England). Structural analysis of the thin-film samples was performed *via* X-ray diffraction (XRD) using a Bruker 8D X-ray diffractometer, equipped with a ceramic tube (Cu Kα, $\lambda = 1.5418$ Å). X-ray photoelectron spectroscopy (XPS, PHI 5000 Versa Probe II, USA) was applied to investigate the chemical state of different types of PVSK and PbI_2 films. The photovoltaic performance was evaluated using a computer-controlled digital source meter (Keithley 2401, USA) under simulated sunlight provided by a commercial solar simulator (PEC-L15, Percell Technologies, Japan) at 1 sun, AM1.5G, with light intensity calibrated by a monocrystalline silicon photodiode (KG3, Oriel, USA). A 0.056 cm^2 photomask was affixed to the front of the PSC to ensure precise control over the illuminated area for small-scale devices. Additionally, the trap-filled limit voltage (V_{TFL}) was determined through space charge limited current (SCLC) measurements using a digital source meter (Keithley 2401, USA), employing a scanning rate of 10 mV s^{-1} within a voltage range of 0 to 4 V.

Results and discussion

Chemical reaction of $MAPbI_3/PbI_2$ and MA^0 in moisture

Four types of $MAPbI_3$ films were investigated in this study, including the primary $MAPbI_3$ film (**Primary-$MAPbI_3$**) used as a control and three secondary $MAPbI_3$ films subjected to different MATM conditions. All MATM processes were carried out in a home-made, custom-designed methylamine liquefaction and crystallization reactor (MALCR, shown in Fig. S1), which features a dual-function chamber that allows for either vacuum evacuation or methylamine treatment to be conducted independently. The first secondary $MAPbI_3$ sample (**2nd-$MAPbI_3$/dry**) was prepared by placing the primary $MAPbI_3$ film into the MALCR chamber, followed by a 10 minutes vacuum treatment to re move moisture from both the film surface and the chamber interior. Afterward, MATM was performed to ensure that the reaction occurred in a moisture-free environment. Following this, the chamber was evacuated to complete the desorption process. This sample is hereafter named **2nd-$MAPbI_3$/wet**. For the third secondary $MAPbI_3$ sample, after undergoing the same MATM process as the previous sample, the film was further heated on a 100 °C hotplate for 10 minutes after removal from the chamber, and this sample is hereafter named **2nd-$MAPbI_3$/wet/heat**. The sample preparation flowchart is illustrated in Fig. 1.

First, crystallinity and phase composition of the investigated $MAPbI_3$ films were analysed using XRD. The XRD patterns were collected and are shown in Fig. 2a. Crystallographic reference data were obtained from the following databases: tetragonal $MAPbI_3$ (COD-4518042),[40] PbO·PbIOH (COD-9017630), PbIOH (COD-9017629),[41] PbO (COD-9012703),[42] and PbI_2 (COD-9009141),[43] which were used to identify the formation of the main perovskite phase and possible impurity phases. **Primary-$MAPbI_3$** exhibits characteristic diffraction peaks at 2θ values of 14.09°, 19.98°, 23.47°, and 28.43°, corresponding to the (110),

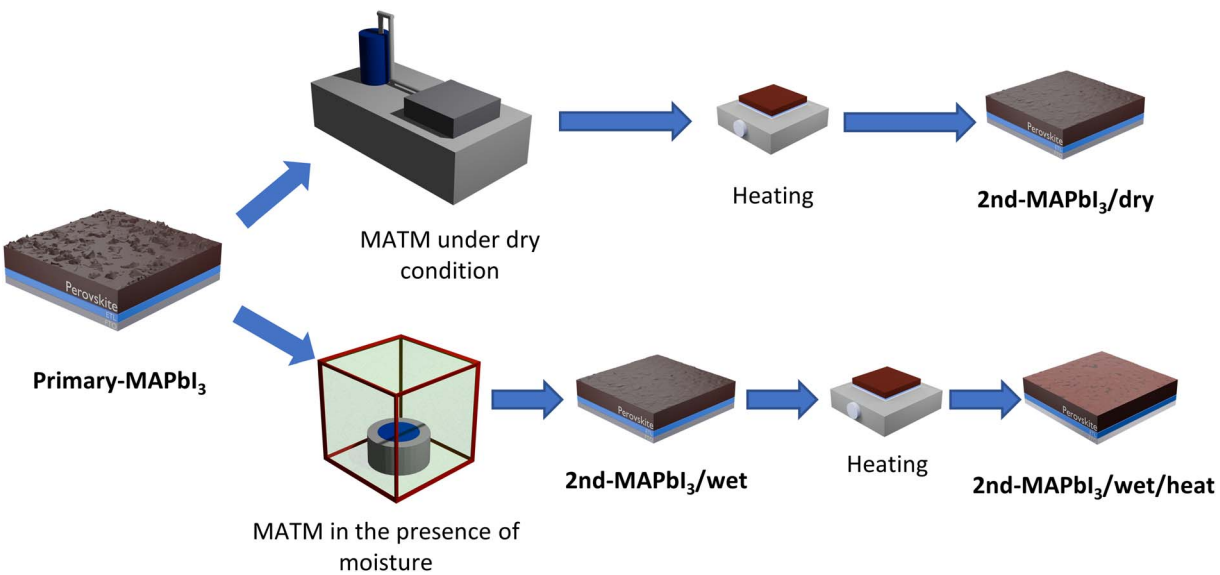

Fig. 1 Schematic diagram of sample preparation.

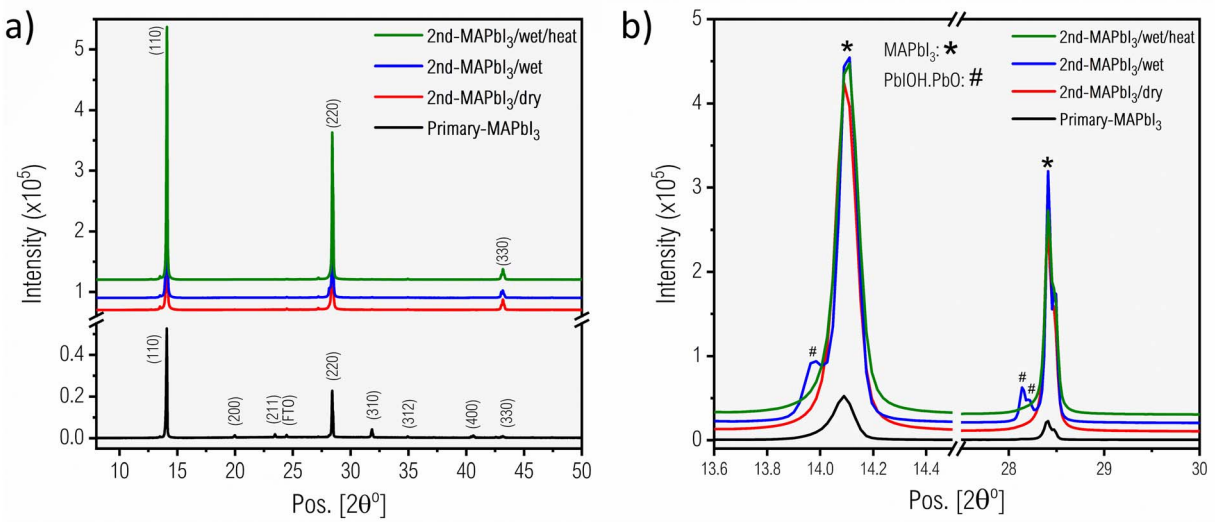

Fig. 2 (a) XRD pattern and (b) zoom-in peak at 14.0° and 28.5° of **Primary-MAPbI$_3$**, **2nd-MAPbI$_3$/dry**, **2nd-MAPbI$_3$/wet** and **2nd-MAPbI$_3$/heat** films.

(200), (211), and (220) planes of polycrystalline $MAPbI_3$, respectively. In contrast, the three secondary $MAPbI_3$ samples display three prominent diffraction peaks at 14.10°, 28.39°, and 43.23°. Notably, the peak corresponding to the (110) plane ($\sim 2\theta = 14°$) is significantly enhanced – by approximately one order of magnitude-consistent with previous reports.[25,31,35,44] The zoom-in XRD pattern of **2nd-MAPbI$_3$/wet** (Fig. 2b) shows extra diffraction peaks at $2\theta = 13.94°$, 28.13°, and 28.33°, which are attributed to PbO·PbIOH, clearly indicating that the presence of moisture during the MATM process can lead to the formation of impurity. This observation is in agreement with the findings reported by Bogachuk *et al.*[39] Although these impurity-related diffraction peaks disappeared for **2nd-MAPbI$_3$/wet/heat**, further investigation is necessary to confirm whether the impurities have been eliminated.

The XPS survey spectrum (Fig. S2) of the $MAPbI_3$ perovskite film reveals peaks at binding energies of 532 eV, 402.5 eV, and 285 eV, corresponding to O 1s, N 1s, and C 1s orbitals, respectively. The characteristic doublet peaks of Pb 4f and I 3d are observed at approximately 138 eV/143 eV and 619 eV/631 eV, respectively, with their expected spin–orbit splitting. To study the chemical modifications in $MAPbI_3$ films under moisture exposure, XPS elemental spectra were analysed. The spectra were calibrated to 285.0 eV, referencing the C 1s binding energy associated with adventitious (aliphatic) carbon or surface-adsorbed hydrocarbon species from the atmosphere.[45] The core-level spectra were fitted using Gaussian line shapes with a Shirley background to ensure accurate peak deconvolution. Fig. S3a displays the XPS spectra of the C 1s core level of investigated samples. All of them exhibit five peaks at 285.0 eV, 286.4 eV, and 286.7 eV. The peak at 285.0 eV is used for calibration and is attributed to adventitious carbon or surface-adsorbed hydrocarbon species. The peak at 286.4 eV can be assigned to C–O or C–OH, which is also associated with surface-adsorbed species. The peak at 286.5 eV can be attributed to the C–N bond of ammonium species in the $MAPbI_3$ film. Fig. S3b shows the XPS of the N 1s core level of $MAPbI_3$ films. All samples contain a single peak at 402.5 eV, corresponding to the C–N bond in $MAPbI_3$ films. The XPS spectra for core level I 3d (Fig. S3c) exhibit two peaks at 619.4 eV and 630.8 eV, corresponding to doublets I $3d_{5/2}$ and I $3d_{3/2}$, which are assigned to Pb–I bonding in the $MAPbI_3$ film.

Fig. 3 shows the Pb 4f core level spectra of investigated $MAPbI_3$ films. **Primary-MAPbI$_3$** (Fig. 3a) and **2nd-MAPbI$_3$/dry** (Fig. 3b) exhibit nearly identical spectra, in which the Pb $4f_{7/2}$ peaks can be further deconvoluted to two contributions at 138.5 eV and 136.8 eV, corresponding to Pb–I, and metallic lead (Pb^0), respectively. For **2nd-MAPbI$_3$/wet** (Fig. 3c) and **2nd-MAPbI$_3$/wet/heat** (Fig. 3d), the Pb $4f_{7/2}$ spectra exhibit a positive shift, allowing for the fitting of an additional peak at approximately 138.7 eV, which is attributed to Pb–OH.[46] A zoom-in observation (Fig. S4) of the 136.0 to 138.0 eV region of the Pb $4f_{7/2}$ spectra reveals the existence of an additional peak at 137.1 eV for **2nd-MAPbI$_3$/wet** and **2nd-MAPbI$_3$/wet/heat**, which is attributed to Pb–O.[47] Fig. 4 depicts the binding ratios from the deconvoluted Pb $4f_{7/2}$ spectra. In **Primary MAPbI$_3$**, the Pb–I bonding characteristic of $MAPbI_3$ accounts for as much as 95.3% of the total lead signal, with the remaining 4.7% consisting of Pb^0. Notably, contributions from Pb–OH and Pb–O species are not detectable. The result for **2nd-MAPbI$_3$/dry** is similar to those of **Primary-MAPbI$_3$**, with contributions from Pb–I, Pb^0 accounting for 96.7%, and 3.3% respectively. This strongly supports the conclusion that MATM conducted under dry conditions specifically repairs film morphology without altering the chemical composition of the $MAPbI_3$ layer. On the contrary, in **2nd-MAPbI$_3$/wet**, the proportion of Pb–I bonds decreases sharply to 56.6%, accompanied by a significant increase in Pb–OH and Pb–O signals to 41.6% and 1.4%, respectively. This clearly confirms the catastrophic chemical transformation that occurs when MATM is conducted in

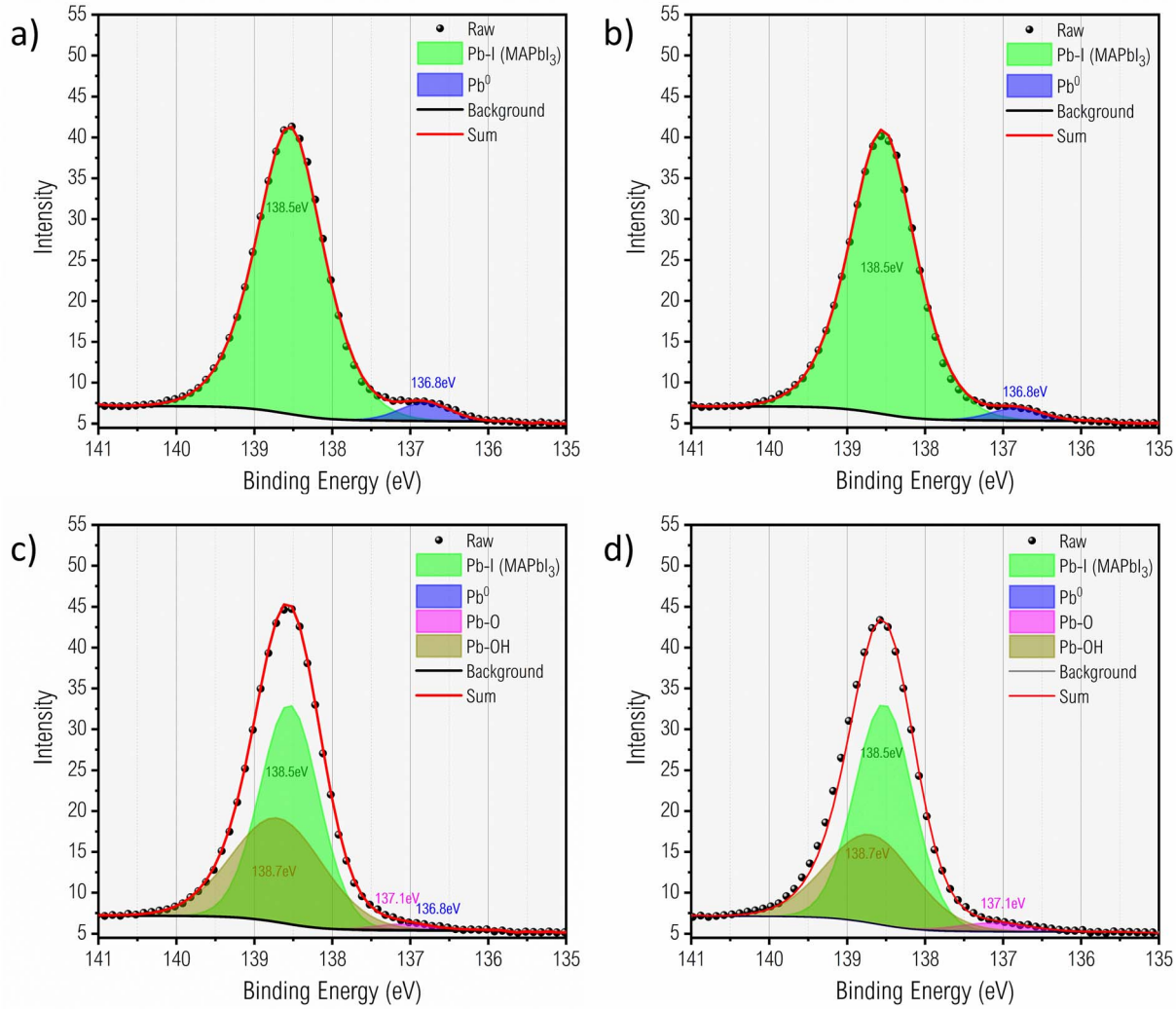

Fig. 3 XPS Pb $4f_{7/2}$ region of (a) **Primary-MAPbI$_3$**, (b) **2nd-MAPbI$_3$/dry**, (c) **2nd-MAPbI$_3$/wet** and (d) **2nd-MAPbI$_3$/heat** films.

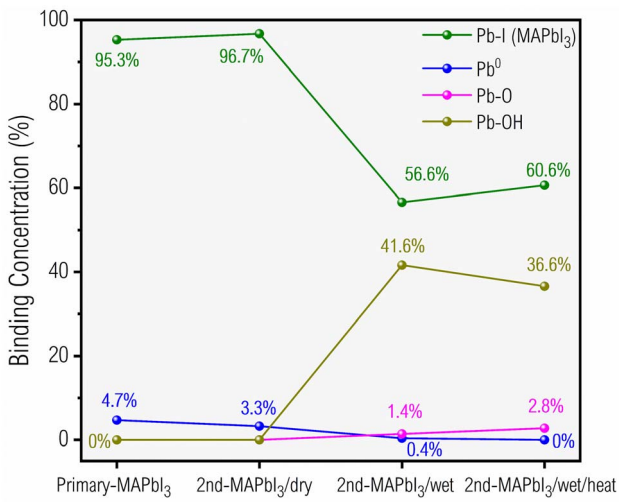

Fig. 4 Pb binding ratios of four types of $MAPbI_3$ films obtained from the deconvoluted Pb $4f_{7/2}$ spectra.

a humid environment: nearly one-third of the $MAPbI_3$ is converted into photoinactive by-products. For **2nd-MAPbI$_3$/wet/heat**, the contributions of Pb–I, Pb–OH, and Pb–O are 60.6%, 36.6%, and 2.8%, respectively. These results indicate that post-heating fails to remove the degradation products formed during the moisture-involved MATM. In fact, the Pb–O signal slightly increases, suggesting further chemical transformation during the heat treatment. This strongly implies that the Pb–OH species in **2nd-MAPbI$_3$/wet** are not merely in the form of $Pb(OH)_2$, but rather exist as photoinactive $MAPbI_{3-y}(OH)_y$-type pseudo-perovskites.

Based on the XPS analysis, we propose the following reaction mechanism when MATM is performed in the presence of moisture. Ideally, MA^0 gas is absorbed onto the $MAPbI_3$ film, inducing a liquid-phase transition to $MAPbI_3 \cdot xMA^0$:

$$xMA^0_{(gas)} + MAPbI_{3(solid)} \rightarrow MAPbI_3 \cdot xMA^0_{(liquid)} \quad (1)$$

When moisture exists, the unpaired electron on the nitrogen atom of MA^0 readily interacts with H_2O, leading to the formation of MAOH:

$$MA^0_{(gas)} + H_2O_{(gas)} \rightarrow MAOH_{(gas)} \quad (2)$$

Water can also react with adsorbed MA^0 to form MAOH-related intermediates:

$$MAPbI_3 \cdot xMA^0_{(liquid)} + xH_2O_{(gas)} \rightarrow MAPbI_3 \cdot xMAOH_{(liquid)} \quad (3)$$

The OH^- then exchanges with the I^- in the liquid intermediate, leading to the formation of the $MAPbI_{3-y}(OH)_y$ intermediate:

$$MAPbI_3 \cdot xMAOH_{(liquid)} \rightarrow MAPbI_{3-y}(OH)_y \cdot (x-y)MAOH_{(liquid)} + yMAI_{(solid)} \quad (4)$$

This intermediate can further degrade into PbIOH and PbO:

$$MAPbI_{3-y}(OH)_y \cdot (x-y)MAOH_{(liquid)} \rightarrow MAPbI_{3-y}(OH)_{y(solid)} + (x-y)MAOH_{(gas)} \quad (5)$$

$$MAPbI_{3-y}(OH)_{y(solid)} \rightarrow yMAI_{(solid)} + yPbIOH_{(solid)} + (1-y)MAPbI_{3(solid)} \quad (6)$$

$$2PbIOH_{(solid)} \rightarrow 2PbO_{(solid)} + H_2O_{(gas)} \quad (7)$$

Since solution-processed $MAPbI_3$ films typically contain unreacted PbI_2,[48–50] we then shifted our focus on the effect of PbI_2 during moisture-involved MATM. Whether and how this residual PbI_2 undergoes transformation during the MATM process remains an intriguing yet explored question. Following the same analytical approach used for $MAPbI_3$, we prepared three types of PbI_2 film samples: **Raw-PbI$_2$**, **PbI$_2$/wet**, and **PbI$_2$/wet/heat**. These correspond to PbI_2 films spin-coated onto glass substrates, films subjected to moisture-involved MATM, and those further treated by post-annealing, respectively. Fig. 5 presents the XRD patterns of the investigated PbI_2 samples, in which the diffraction pattern of **Raw-PbI$_2$** displays characteristic peaks at 12.68°, 22.99°, 25.45°, 33.66°, 39.54°, and 41.70°, corresponding to (001), (010), (002), (120), (121) orientations of PbI_2 polycrystals. For **PbI$_2$/wet**, additional peaks emerge at 14.11°, 28.39°, 31.87°, 40.80°, and 43.26°. Notably, the peak at 14.11° closely aligns with the (110) characteristic diffraction of $MAPbI_3$, strongly implying the formation of $MAPbI_2OH$ pseudo-perovskite.[51] Other additional peaks of **PbI$_2$/wet** at 28.39°, 31.87°, 40.80°, and 43.26° are associated with lead oxide and hydroxide compounds, specifically PbO·PbIOH, PbO, and PbIOH. Upon heating (**PbI$_2$/wet/heat**), the peak at 14.11° disappears, whereas the peak corresponding to PbO·PbIOH (28.2°) persists.

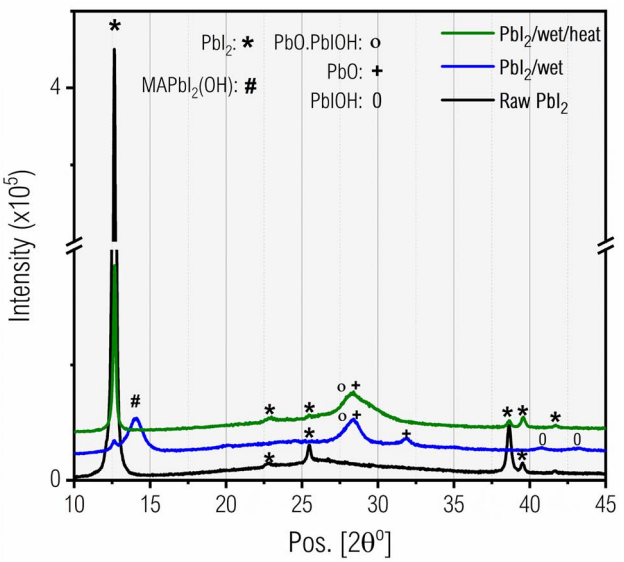

Fig. 5 XRD patterns of **Raw-PbI$_2$**, **PbI$_2$/wet** and **PbI$_2$/wet/heat** films.

XPS survey spectra of investigated PbI_2 films are shown in Fig. S5. Similarly, C 1s, O 1s, Pb 4f and I 3d orbitals are clearly identified, in which Pb 4f elemental spectra are deconvoluted for discussion. As shown in Fig. 6a, **Raw-PbI$_2$** exhibits a dominant peak at 138.9 eV, attributed to the Pb–I in PbI_2, along with a minor peak at 137.1 eV (shown in Fig. S6), corresponding to Pb–O in the $PbI_2(DMSO)_x$ complex, respectively.[52–54] For **PbI$_2$/wet** (Fig. 6b), a shift in binding energy to 138.76 eV is observed, enabling the fitting of an additional peak at 138.7 eV, which corresponds to Pb–OH bonding. Upon heating (**PbI$_2$/wet/heat**), the removal of MAOH reduces the Pb–OH contribution, causing the main peak to revert to 138.84 eV (Fig. 6c). Fig. 6d summarizes the bonding ratio of lead species in the PbI_2 film, which is normalized by the area of Pb $4f_{7/2}$ peak. In the **Raw-PbI$_2$** films, the Pb–I bonds dominate, accounting for 96.3%, with a small fraction of Pb–O bonds as 3.7%. In contrast, the **PbI$_2$/wet** film shows a dramatic decrease in Pb–I bonding to 53.4%, accompanied by a significant increase in Pb–OH bonding to 40%, and a slight rise in Pb–O bonding to 6.6%, indicating the formation of lead hydroxide and lead oxide in the **PbI$_2$/wet** film. Upon annealing (the **PbI$_2$/wet/heat**), the Pb–I bond ratio increases moderately to 66.9%, while those Pb–OH and Pb–O decrease modestly to 27.5% and 5.6%, respectively. These results indicate that the interaction of the PbI_2 film and MA^0 under humid conditions leads to the formation of Pb–OH and Pb–O, and both will remain in the resultant film, even with post-heating treatment.

Similarly, possible reactions involved in MATM on the PbI_2 film in the presence of moisture are proposed below. Ideally, PbI_2 chemisorbs MA^0 to form a liquid-phase $PbI_2 \cdot xMA^0$ complex:

$$xMA^0_{(gas)} + PbI_{2(solid)} \rightarrow PbI_2 \cdot xMA^0_{(liquid)} \quad (8)$$

However, water can also react with MA^0, as mentioned previously in reaction (2). Or with the adsorbed MA^0 intermediate, eventually forming $PbI_2 \cdot xMAOH$:

$$PbI_2 \cdot xMA^0_{(liquid)} + H_2O_{(gas)} \rightarrow PbI_2 \cdot xMAOH_{(liquid)} \quad (9)$$

The OH^- can exchange with I^- to produce pseudo perovskite $MAPbI_2OH$ and the $PbI_2 \cdot MAOH$ intermediate:

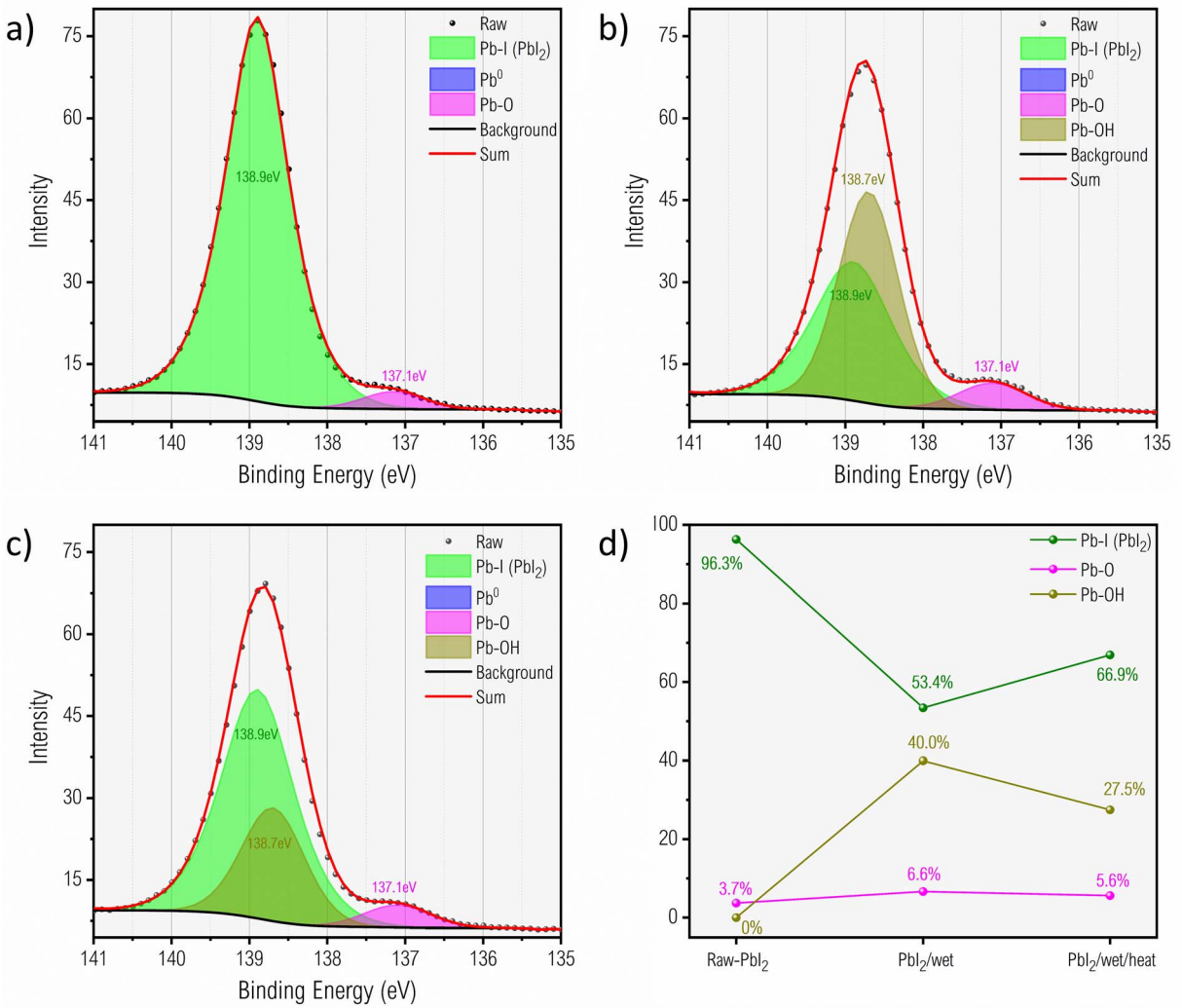

Fig. 6 (a)–(c) XPS Pb $4f_{7/2}$ regions and (d) binding ratios of **Raw-PbI_2**, **PbI_2/wet**, **PbI_2/wet/heat** films.

$$PbI_2{\cdot}xMAOH_{(liquid)} \rightarrow y MAPbI_2OH_{(solid)} + (1-y)PbI_2{\cdot}(x-y)MAOH_{(liquid)} \quad (10)$$

The pseudo perovskite and intermediate can further decompose into PbIOH and PbO:

$$PbI_2{\cdot}(x-y)MAOH_{(liquid)} \rightarrow PbI_{2(solid)} + (x-y)MAOH_{(gas)} \quad (11)$$

$$MAPbI_2OH_{(solid)} \rightarrow MAI_{(solid)} + PbIOH_{(solid)} \quad (12)$$

PbIOH further decomposes into PbO and H_2O as mentioned above in reaction (7).

Morphology analysis

Fig. 7 illustrates the SEM and AFM topographies of the investigated $MAPbI_3$ films. The **Primary-$MAPbI_3$** film (Fig. 7a) consists of large $MAPbI_3$ grains ranging from 500 to 2000 nm, rendering a rough surface with a surface roughness (S_a) of 66.7 nm. All MA^0-treated samples reveal significantly reduced surface roughness. S_a of **2nd-$MAPbI_3$/dry**, **2nd-$MAPbI_3$/wet** and **2nd-$MAPbI_3$/wet/heat** is 13.96 nm, 12.58 nm and 14.16 nm, respectively. Due to the inherent dissolution–recrystallization behaviour of MATM, the significant reduction in S_a values observed in the three MATM-treated samples is expected, as this mechanism naturally smoothens the $MAPbI_3$ film surface. The top-view images of **2nd-$MAPbI_3$/dry** (Fig. 7b) and **2nd-$MAPbI_3$/wet** (Fig. 7c) show almost no discernible differences, either in SEM morphology or S_a values. In fact, this is not favourable for the practical operation of MATM, as the chemical composition of **2nd-$MAPbI_3$/wet** has already deteriorated, as discussed above. Its seemingly smooth and a uniform surface morphology may lead to a misleading assessment of film quality. On the other hand, a closer inspection of the **2nd-$MAPbI_3$/wet/heat** sample (Fig. 7d) reveals the presence of prominent cracks, indicating that the moisture content during MATM may still affect the integrity of the resultant film. Based on the preceding discussion, we have reason to believe that the outgassing of MAOH during the post-heating process of the **2nd-$MAPbI_3$/wet** sample is the primary cause of the observed cracking.

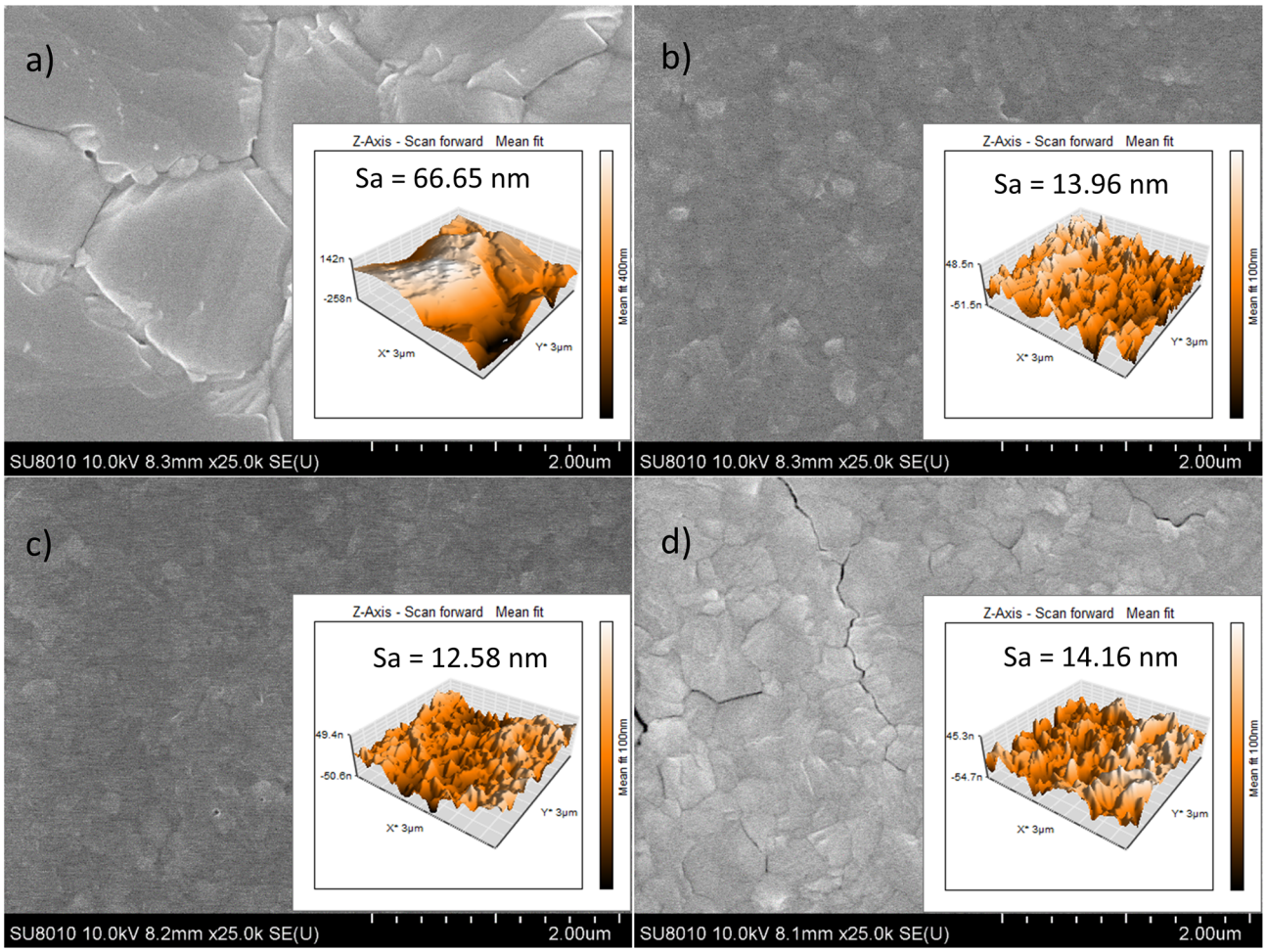

Fig. 7 SEM topographic view and AFM of PVSK films: (a) **Primary-MAPbI$_3$**, (b) **2nd-MAPbI$_3$/dry**, (c) **2nd-MAPbI$_3$/wet** and (d) **2nd-MAPbI$_3$/wet/heat** films.

Optoelectrical properties

Fig. 8a presents the UV-vis absorption spectra of **Primary-MAPbI$_3$** and **2nd-MAPbI$_3$** films. The three **2nd-MAPbI$_3$** films exhibit similar absorbance in the 650–900 nm range, whereas the **Primary-MAPbI$_3$** film demonstrates a higher overall absorbance. The reduced absorbance observed in the **2nd-MAPbI$_3$** films is attributed to their lower surface roughness, which reduces light scattering. The Tauc-plot derived from the absorption spectra, shown in Fig. 8b, indicates that the optical bandgap (E_g) of the **Primary-MAPbI$_3$** film is 1.591 eV. In contrast, the **2nd-MAPbI$_3$** films exhibit a slightly higher E_g of approximately 1.600 eV. The change is small and is likely due to the preferred (110) crystallographic orientation in the $MAPbI_3$ PVSK structure.[24,31]

Space-charge-limited current (SCLC) measurements were conducted to quantitatively assess the impact on trap-filling limited voltage (V_{TFL}) and trap density (N_t). The corresponding SCLC curves are presented in Fig. 8c. The V_{TFL} value is identified at the transition point between the ohmic and trap-filled limit (TFL) regions, while N_t is determined using the following equation:

$$N_t = 2\varepsilon\varepsilon_o \frac{V_{TFL}}{eL^2}$$

In this equation, e represents the elementary charge (1.602×10^{-19} C), ε_o denotes the vacuum permittivity (8.854×10^{-12} F m^{-1}), ε corresponds to the relative dielectric constant of $MAPbI_3$ (32), and L signifies the thickness of the perovskite film. A summary of the V_{TFL} and N_t values for the examined samples is provided in Table 1. The **Primary-MAPbI$_3$** exhibits a V_{TFL} of 0.770 V and a N_t of 1.42×10^{16} cm^{-3}. **2nd-MAPbI$_3$/dry** demonstrates a reduced V_{TFL} (0.715 V) and N_t (1.25×10^{16} cm^{-3}), suggesting that the quality of the film is enhanced by the MATM process, which is consistent with previous studies.[31] However, at **2nd-MAPbI$_3$/wet**, both V_{TFL} and N_t exhibit a significant increase, reaching 1.14 V and 1.99×10^{16} cm^{-3}, respectively. This indicates that impurities such as $MAPbI_2OH$, PbO, and PbIOH introduce a higher density of defect-trap states within the crystal lattice. Following post-heating treatment (**2nd-MAPbI$_3$/wet/heat**), a substantial portion of MAOH is removed; however, residual PbO and PbIOH persist in the perovskite film, contributing to an elevated defect density, measured at 1.486×10^{16} cm^{-3}.

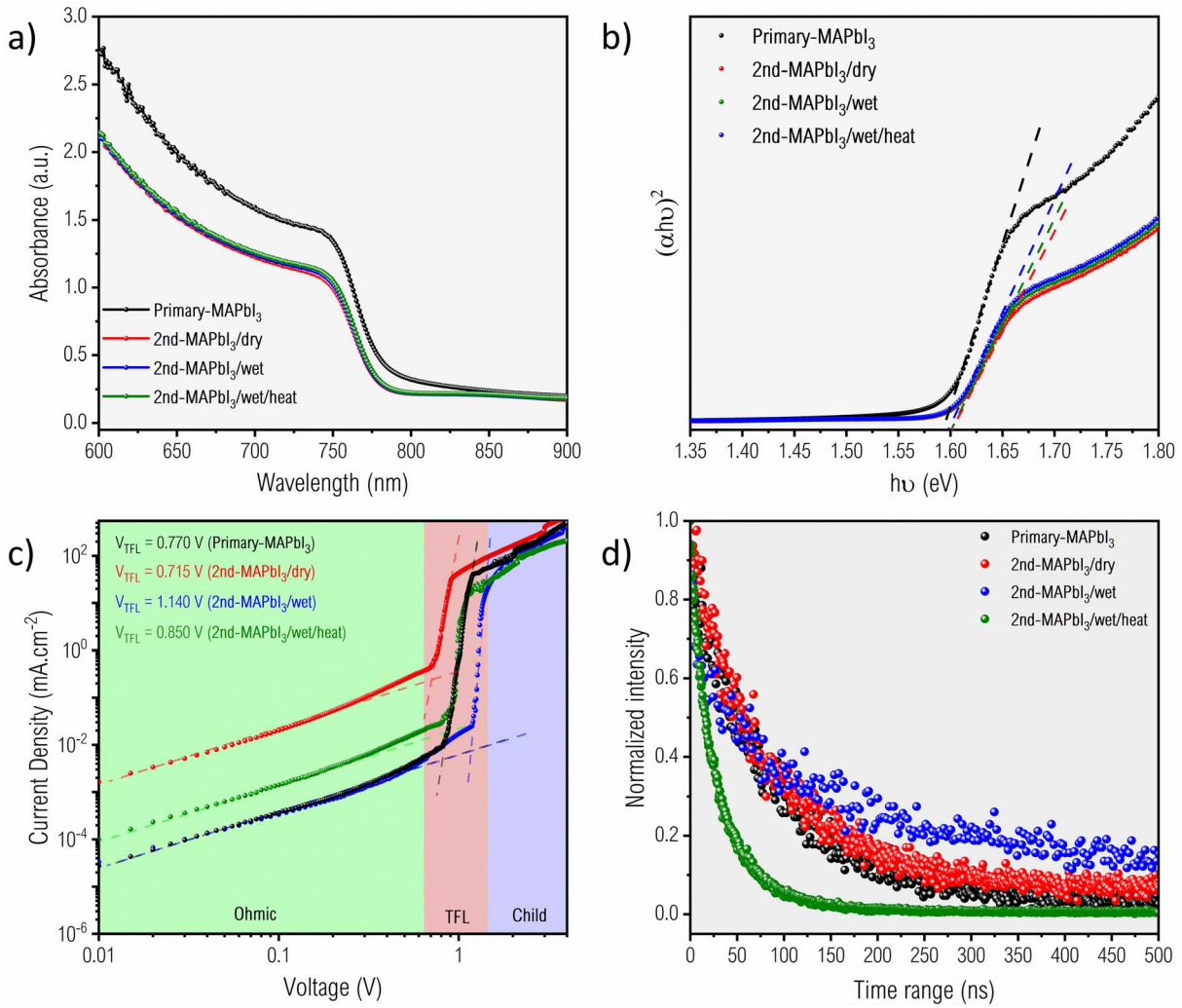

Fig. 8 (a) UV-vis absorption spectra, (b) Tauc-plot, (c) the SCLC curves and (d) the TRPL spectra of the glass/Al_2O_3/PVSK film of **Primary-MAPbI$_3$**, **2nd-MAPbI$_3$/dry**, **2nd-MAPbI$_3$/wet** and **2nd-MAPbI$_3$/wet/heat** films.

The carrier lifetime of the investigated samples was probed using time-resolved photoluminescence (TRPL). The TRPL data shown in Fig. 8d were fitted with the following bi-exponential function:

$$I(t) = A_1 e^{-\frac{t}{\tau_1}} + A_2 e^{-\frac{t}{\tau_2}} + I_0$$

where A_1 and A_2 represent the pre-exponential factors, while I_0 is a constant accounting for the background signal. The short lifetime (τ_1) is primarily associated with non-radiative surface recombination, whereas the long lifetime (τ_2) corresponds to bulk radiative recombination within the PVSK film.

We subsequently calculated the average carrier lifetime using the amplitude-weighted method:[55]

$$\tau_{avg} = \frac{\sum(A_i\tau_i)}{\sum(A_i)}$$

Table 1 Optoelectronic parameters of various $MAPbI_3$ films

	Primary-MAPbI$_3$	2nd-MAPbI$_3$/dry	2nd-MAPbI$_3$/wet	2nd-MAPbI$_3$/wet/heat
V_{TFL} (V)	0.770	0.715	1.14	0.850
N_t ($\times 10^{16}$ cm^{-3})	1.421	1.250	1.993	1.486
τ_1 (ns)	8.69	31.08	3.55	12.15
A_1 (%)	11.19	26.05	43.33	36.52
τ_2 (ns)	93.19	108.46	120.71	39.23
A_2 (%)	88.81	73.95	56.67	63.48
τ_{avg} (ns)	83.74	88.30	69.95	29.34

The results are summarized in Table 1. The **Primary-MAPbI$_3$** film shows a τ_1 of 8.69 ns and a τ_2 of 93.19 ns, with an average lifetime (τ_{avg}) of 83.74 ns. For the **2nd-MAPbI$_3$/dry** sample, both τ_1, τ_2 and τ_{avg} increase to 31.08 ns, 108.46 ns, and 88.30 ns, respectively, indicating that when the MATM process proceeds without moisture interference, both film integrity and trap density are improved.

For the moisture-affected samples (**2nd-MAPbI$_3$/wet** and **2nd-MAPbI$_3$/wet/heat**), a shorter τ_{avg} is observed, suggesting that the moisture-induced photovoltaic-inactive hydrated byproducts adversely influence carrier lifetime and consequently degrade photovoltaic properties. Interestingly, the **2nd-MAPbI$_3$/wet** film exhibits the longest τ_2 (120.71 ns) but simultaneously the shortest τ_1 (3.55 ns) among all samples. We attribute this phenomenon to moisture-induced, photovoltaic-inactive phases forming electrically isolated high-quality domains, which artificially inflate the average PL lifetime – resulting in a pseudo-long lifetime – while the majority of photogenerated carriers still undergo rapid non-radiative interfacial recombination before reaching the charge-transport layers, as evidenced by the shortest τ_1. Combining TRPL and SCLC analysis, it is evident that the existence of impurities such as $MAPbI_2OH$, PbO, and PbIOH formed during moisture-involved MATM leads to the reduction in electron lifetime. As for **2nd-MAPbI$_3$/wet/heat**, both τ_1 and τ_2 became shorter even compared with **Primary-MAPbI$_3$**, saying that even with a post-heating treatment, the damage of $MAPbI_3$ due to improper MATM is difficultly reverted. We attribute this is because although post-heating removes certain OH-species, the post-heating itself also induces fast diffusion of impurities from the surface to the bulk film. Such an effect increases trap density and eventually shortens the electron lifetime of the entire PVSK film.

Photovoltaic performance

Table 2 and Fig. S7 illustrate the photovoltaic statistics of the PSC made with the investigated $MAPbI_3$ films. *J–V* curves of the best-performing devices are plotted in Fig. 9a, in which the best **Primary-MAPbI$_3$**-based device exhibited a PCE of 16.55%, with a short-circuit current density (J_{SC}) of 21.41 mA cm^{-2}, an open-circuit voltage (V_{OC}) of 1.01 V, and a fill factor (FF) of 76.30%. For **2nd-MAPbI$_3$/dry**-based devices, improved PVSK film quality led to an increase in all photovoltaic parameters. The best-performing PSC employed with **2nd-MAPbI$_3$/dry** showed a J_{SC}, V_{OC}, and FF of 23.78 mA cm^{-2}, 1.04 V, and 78.71%, respectively, resulting in an improved PCE of 19.48%. If the MATM were performed with moisture interference, PCEs of the devices declined considerably to 16.11% and 18.74%, for the case of **2nd-MAPbI$_3$/wet** and **2nd-MAPbI$_3$/wet/heat**, respectively. This result once again highlights the critical importance of environmental conditions during MATM of $MAPbI_3$ films. In particular, in the presence of moisture, although the surface morphology can still be effectively smoothened, the formation of undesirable by-products significantly deteriorates the optoelectronic properties of the resultant $MAPbI_3$ films, ultimately leading to decreased device performance rather than improvement.

The hysteresis index (HI), which is defined as:

$$\mathrm{HI} = \frac{\left(\mathrm{PCE}_{\mathrm{reverse\ \ scan}} - \mathrm{PCE}_{\mathrm{forward\ \ scan}}\right)}{\mathrm{PCE}_{\mathrm{reverse\ \ scan}}}$$

is a key indicator for evaluating trap-assisted recombination, surface charge recombination, and ion migration in PSCs. As can be seen in Fig. S8 and Table S1, **Primary-MAPbI$_3$** exhibited a relatively large HI of 0.30, confirming its significant hysteresis behavior. In contrast, all three types of **2nd-MAPbI$_3$** devices demonstrated substantially reduced HI values (0.07–0.09), highlighting that the liquefaction–recrystallization mechanism of MATM effectively improves film uniformity and compactness, leading to suppressed hysteresis. Among the three **2nd-MAPbI$_3$** devices, the **2nd-MAPbI$_3$/dry** film showed the lowest HI compared to the **2nd-MAPbI$_3$/wet** and **2nd-MAPbI$_3$/wet/heat** films. This increase in hysteresis for the latter two devices is primarily attributed to the presence of photovoltaic-inactive impurities introduced by moisture during MATM, which results in higher defect density within the perovskite film.

Overall, based on the current results, improved film compactness appears to be the dominant factor in hysteresis suppression, which is a fundamental benefit provided by the MATM process. With further refinement of MATM operation—particularly by eliminating moisture interference—the enhancement in film quality and corresponding hysteresis reduction can be further strengthened.

Fig. 9b shows the incident photon-to-electron conversion efficiency (IPCE) spectra of the four investigated devices. The integrated J_{SC} values are 19.47 mA cm^{-2} for **Primary-MAPbI$_3$**, 21.50 mA cm^{-2} for **2nd-MAPbI$_3$/dry**, 19.28 mA cm^{-2} for **2nd-MAPbI$_3$/wet**, and 20.50 mA cm^{-2} for **2nd-MAPbI$_3$/wet/heat**,

Table 2 Photovoltaic parameters of various $MAPbI_3$ films (based on 15 cells)

Device	EQE-J_{SC} (mA cm^{-2})		J_{SC} (mA cm^{-2})	V_{OC} (V)	FF (%)	PCE (%)	HI
Primary-MAPbI$_3$	19.47	Champion	21.41	1.01	76.30	16.55	0.30
		Average	22.36 ± 0.68	0.99 ± 0.02	72.03 ± 3.55	15.91 ± 0.63	
2nd-MAPbI$_3$/dry	21.50	Champion	23.78	1.04	78.71	19.48	0.07
		Average	22.97 ± 0.55	1.04 ± 0.02	77.63 ± 1.52	18.67 ± 0.56	
2nd-MAPbI$_3$/wet	19.28	Champion	21.19	1.01	75.81	16.11	0.09
		Average	20.98 ± 0.86	1.00 ± 0.01	67.04 ± 4.43	14.10 ± 0.79	
2nd-MAPbI3/wet/heat	20.50	Champion	22.64	1.06	77.86	18.74	0.08
		Average	22.49 ± 0.31	1.05 ± 0.02	73.27 ± 2.74	17.26 ± 0.80	

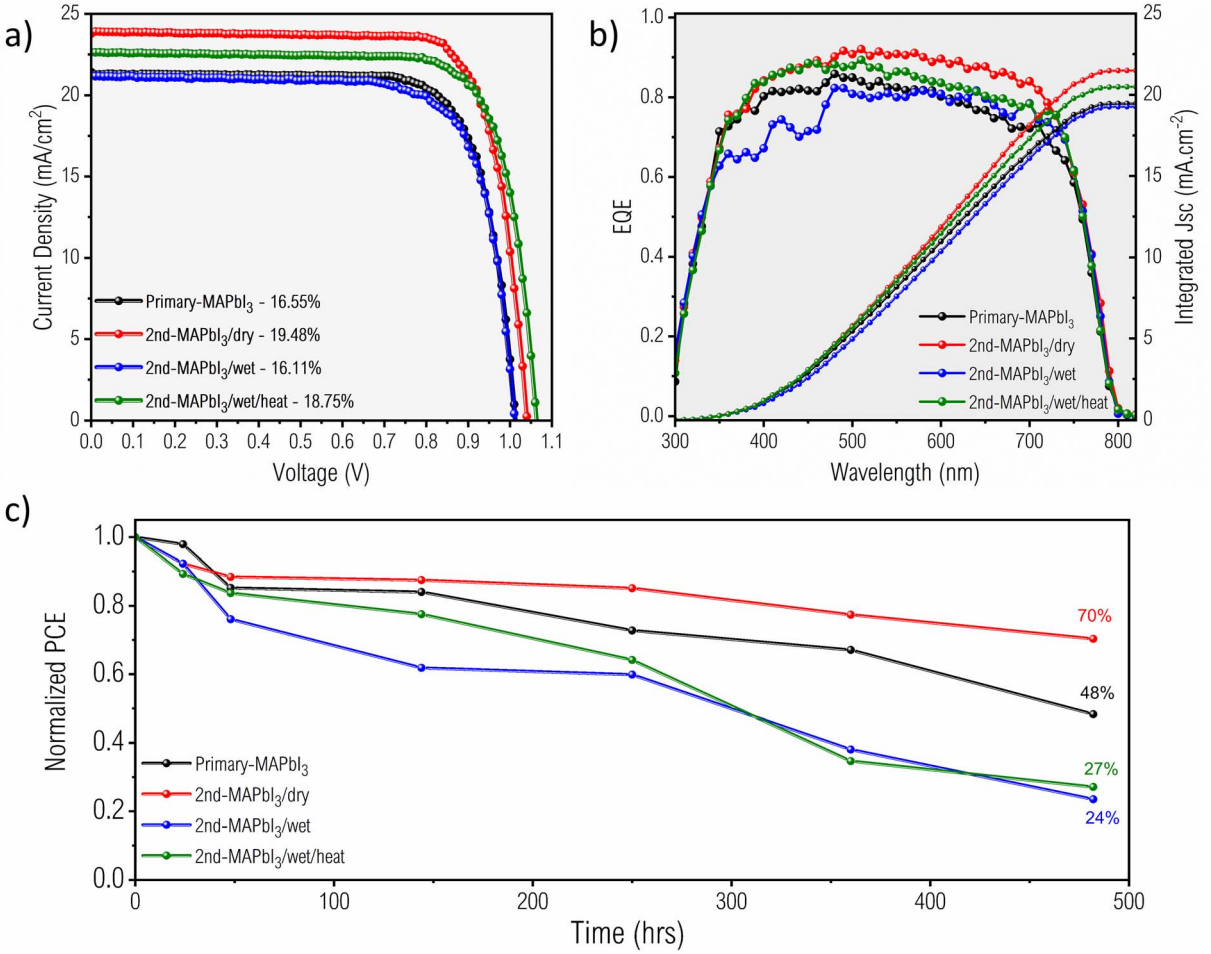

Fig. 9 (a) The best performance *J*–*V* curves of perovskite $MAPbI_3$ devices with **Primary-$MAPbI_3$** and **2nd-$MAPbI_3$** (backward scan); (b) EQE and integrated J_{SC} of perovskite $MAPbI_3$ devices and (c) stability of devices made using **Primary-$MAPbI_3$** and **2nd-$MAPbI_3$** films.

which are consistent with the trend observed in the *J*–*V* characteristics.

For the **2nd-$MAPbI_3$/wet** device, the reduced integrated J_{SC} can be attributed to two major factors. First, the EQE is significantly suppressed in the 300–450 nm region, suggesting enhanced surface recombination or parasitic absorption at the transport-layer/perovskite interface (*e.g.*, TiO_2/PVSK).[56] This is supported by the shortened TRPL lifetime ($\tau_1 \approx 3.55$ ns) and pronounced SSPL quenching in the **2nd-$MAPbI_3$/wet** films. A slight suppression in this region is also found for **Primary-$MAPbI_3$**, indicating the presence of residual surface recombination. Second, the suppressed EQE in the 500–750 nm region indicates an increase in bulk recombination due to the presence of intrinsic defects in the perovskite film. This interpretation is further validated by the results from SSPL, SCLC, and TRPL characterization.

Overall, MATM performed under dry conditions effectively improves perovskite film morphology, heals defects, and reduces trap density, thereby contributing to the enhancement of photovoltaic performance.

Notably, although the **2nd-$MAPbI_3$** films exhibit a reduced average grain size compared with the **Primary-$MAPbI_3$** films, their device performance is significantly improved. This observation contrasts with the widely accepted understanding that larger perovskite grains are beneficial for reducing defect density and enhancing optoelectronic properties. Such a counter-intuitive result highlights that grain size is not the

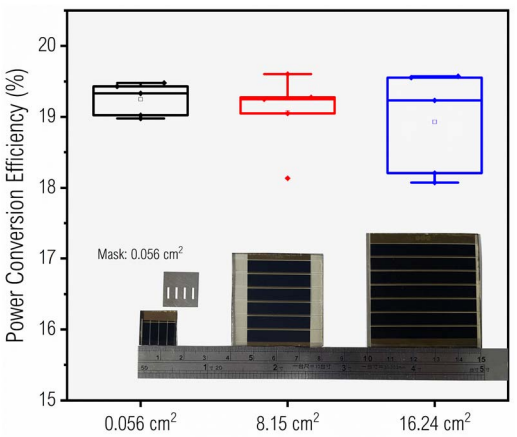

Fig. 10 Performance of small devices and module devices.

Table 3 Photovoltaic parameters of **2nd-MAPbI$_3$/dry** devices with different active areas (based on 5 devices)

PSC		J_{SC} (mA cm^{-2})	V_{OC} (V)	FF (%)	PCE (%)
Cell with an active area of 0.056 cm^2	Champion	23.78	1.04	78.71	19.48
	Average	23.43 ± 0.38	1.04 ± 0.02	78.57 ± 1.05	19.25 ± 0.21
Module with an active area of 8.15 cm^2	Champion	3.85	6.73	75.66	19.60
	Average	3.81 ± 0.11	6.69 ± 0.09	74.77 ± 1.48	19.06 ± 0.50
Module with an active area of 16.24 cm^2	Champion	3.23	7.87	77.00	19.57
	Average	3.22 ± 0.06	7.47 ± 0.30	78.78 ± 1.61	18.93 ± 0.66

sole dominant factor determining device performance. Instead, the MATM improves crystallographic quality, film compactness and suppressed defect formation through a liquefaction–recrystallization mechanism. These improvements collectively facilitate enhanced charge extraction and reduced non-radiative recombination losses, ultimately leading to superior photovoltaic performance despite the smaller grain size. Our results therefore reinforce that structural coherence, defect passivation, and film continuity can outweigh grain-size effects in governing PSC efficiency.

To evaluate the impact of moisture during MATM on the stability of PSCs, we fabricated both **Primary-MAPbI$_3$** and **2nd-MAPbI$_3$** films, storing them under controlled humidity conditions (15–25%) without encapsulation. As shown in Fig. 9c, the long-term stability of PSCs fabricated from **Primary-MAPbI$_3$**, **2nd-MAPbI$_3$/dry**, **2nd-MAPbI$_3$/wet**, and **2nd-MAPbI$_3$-MAPbI$_3$/wet/heat** was systematically compared. After more than 480 hours of ambient storage, PSCs based on **2nd-MAPbI$_3$/dry** films retained 70% of their initial power conversion efficiency (PCE), while devices based on **Primary-MAPbI$_3$** retained only 48%. In contrast, devices that underwent MA^0 treatment in the presence of moisture and those subjected to subsequent heating exhibited markedly accelerated degradation, retaining only 24% and 27% of their initial PCE, respectively.

These results indicate that the incorporation of impurities during the moisture-influenced MATM process significantly accelerates device degradation. Furthermore, the MATM process conducted within the MALCR system, which functions as a moisture-isolated environment, yields enhanced device stability compared to PSCs fabricated using untreated **Primary-MAPbI$_3$** films.

Upscaling PSC using moisture-free MATM

After confirming that proper implementation of MATM can simultaneously enhance both the efficiency and stability of PSCs, we further investigated another critical advantage of this technique: its applicability in the fabrication of large-area perovskite solar modules. In addition to the laboratory-scale small-area devices (0.056 cm^2), we progressively scaled up the active area to 8.15 cm^2 (a 4.0 cm × 4.0 cm module consisting of six sub-cells in series) and 16.24 cm^2 (a 5.0 cm × 5.0 cm module comprising seven sub-cells in series).

Fig. 10 and Table 3 summarize the performance statistics of PSCs with various active areas. Remarkably, under identical device architecture, material composition, and processing conditions, the PCE remained essentially unchanged across different device scales. The laboratory-scale small-area cell exhibited a PCE of 19.68%, while the 8.15 cm^2 and 16.24 cm^2 modules achieved PCEs of 19.60% and 19.57%, respectively. This demonstrates a truly lossless scaling process and represents a significant milestone in the upscaling of high-performance PSC modules.

Conclusions

This study systematically elucidates the impact of environmental moisture on the MATM of MA-based perovskite films and its implications for scalable PSC manufacturing. We demonstrate that uncontrolled humidity during MATM induces the formation of photoinactive by-products such as PbO, PbIOH, and MAPbI$_2$OH, which significantly deteriorate the film's crystallinity, increase trap-state density, and shorten carrier lifetimes. More importantly, the formation of these by-products is uncontrollable, which significantly undermines the feasibility and yield of large-area MATM processing. These defects not only compromise photovoltaic performance but also severely accelerate device degradation. In contrast, performing MATM under dry conditions effectively preserves the liquefaction–recrystallization benefits while preventing deleterious side reactions. Devices treated under dry conditions exhibit a superior PCE of 19.48% and improved long-term stability than a control device with an initial 16.67% PCE. We further demonstrated the scalability of the moisture-free MATM protocol by successfully increasing the device area from 0.056 cm^2 to 16.24 cm^2 without statistical loss in PCE. This clearly highlights the tremendous potential of properly implemented MATM for the fabrication of large-area perovskite films.

Author contributions

Tzu-Chien Wei supervised the study. Duc-Anh Le conceived the idea, designed the experiments, and wrote the first manuscript draft. Both authors contributed to the writing and revision.

Conflicts of interest

There are no conflicts to declare.

Data availability

The data supporting this article have been included as part of the SI. More raw data are available from the corresponding

author on reasonable request. See DOI: https://doi.org/10.1039/d5el00143a.

Acknowledgements

This project has received funding from the National Science and Technology Council, Taiwan, ROC (114-2811-E-007-021) and a grant from National Tsing-Hua University, Taiwan, ROC (113Q2750E1).

Notes and references

1 J. S. Manser and P. V. Kamat, *Nat. Photonics*, 2014, **8**, 737–743.
2 S. De Wolf, J. Holovsky, S.-J. Moon, P. Löper, B. Niesen, M. Ledinsky, F.-J. Haug, J.-H. Yum and C. Ballif, *J. Phys. Chem. Lett.*, 2014, **5**, 1035–1039.
3 S. D. Stranks, G. E. Eperon, G. Grancini, C. Menelaou, M. J. P. Alcocer, T. Leijtens, L. M. Herz, A. Petrozza and H. J. Snaith, *Science*, 2013, **342**, 341–344.
4 G. Xing, N. Mathews, S. Sun, S. S. Lim, Y. M. Lam, M. Grätzel, S. Mhaisalkar and T. C. Sum, *Science*, 2013, **342**, 344–347.
5 G. E. Eperon, S. D. Stranks, C. Menelaou, M. B. Johnston, L. M. Herz and H. J. Snaith, *Energy Environ. Sci.*, 2014, **7**, 982–988.
6 The National Renewable Energy Laboratory, https://www.nrel.gov/pv/cell-efficiency.html.
7 A. Kojima, K. Teshima, Y. Shirai and T. Miyasaka, *J. Am. Chem. Soc.*, 2009, **131**, 6050–6051.
8 M. Saliba, J.-P. Correa-Baena, C. M. Wolff, M. Stolterfoht, N. Phung, S. Albrecht, D. Neher and A. Abate, *Chem. Mater.*, 2018, **30**, 4193–4201.
9 Y. Galagan, F. Di Giacomo, H. Gorter, G. Kirchner, I. de Vries, R. Andriessen and P. Groen, *Adv. Energy Mater.*, 2018, **8**, 1801935.
10 A. T. Barrows, A. J. Pearson, C. K. Kwak, A. D. F. Dunbar, A. R. Buckley and D. G. Lidzey, *Energy Environ. Sci.*, 2014, **7**, 2944–2950.
11 H. Cai, X. Liang, X. Ye, J. Su, J. Guan, J. Yang, Y. Liu, X. Zhou, R. Han, J. Ni, J. Li and J. Zhang, *ACS Appl. Energy Mater.*, 2020, **3**, 9696–9702.
12 Q. Yao, Z. Gu, C. Chen, Y. Jiang, Z. Su, J. Wang, T. Niu, T. Pan, Y. Xia, L. Zheng, X. Gao, J. Zhang, X. Duan, L. Chao and Y. Chen, *Angew. Chem., Int. Ed.*, 2025, **64**, e202501350.
13 H. Eggers, F. Schackmar, T. Abzieher, Q. Sun, U. Lemmer, Y. Vaynzof, B. S. Richards, G. Hernandez-Sosa and U. W. Paetzold, *Adv. Energy Mater.*, 2020, **10**, 1903184.
14 H. Wang, W. Zeng and R. Xia, *Thin Solid Films*, 2018, **663**, 9–13.
15 A. D. Taylor, Q. Sun, K. P. Goetz, Q. An, T. Schramm, Y. Hofstetter, M. Litterst, F. Paulus and Y. Vaynzof, *Nat. Commun.*, 2021, **12**, 1878.
16 P. Chen, X. Ma, Z. Wang, N. Yang, J. Luo, K. Chen, P. Liu, W. Xie and Q. Hu, *Phys. Chem. Chem. Phys.*, 2024, **26**, 14874–14882.
17 Q. Chen, H. Zhou, Z. Hong, S. Luo, H.-S. Duan, H.-H. Wang, Y. Liu, G. Li and Y. Yang, *J. Am. Chem. Soc.*, 2014, **136**, 622–625.
18 S. Zhang, Y. Ge, X. Qin, X. Wang, T. Tao, L. Yu, X. Song, Y. Jiang and C. Xia, *Adv. Funct. Mater.*, 2025, **35**, 2418968.
19 Z. Su, Y. Sun, B. Yu and H. Yu, *ACS Appl. Mater. Interfaces*, 2024, **16**, 43489–43497.
20 A. Perveen, Y. Xu, S. M. Abubakar, P. Sellan, W. Xin, F. Saeed, S. Hussain, B. S. Bae, J. Zhou, Y. Zhu and W. Lei, *Adv. Opt. Mater.*, 2024, **12**, 2302918.
21 Z. Xiao, Q. Dong, C. Bi, Y. Shao, Y. Yuan and J. Huang, *Adv. Mater.*, 2014, **26**, 6503–6509.
22 Y. Tu, J. Wu, X. He, P. Guo, T. Wu, H. Luo, Q. Liu, K. Wang, J. Lin, M. Huang, Y. Huang, Z. Lan and S. Li, *J. Mater. Chem. A*, 2017, **5**, 4376–4383.
23 M. Chen, Z. Qin, Z. Zhang, Y. Wang and L. Han, *Energy Environ. Sci.*, 2025, **18**, 5952–5960.
24 Y. Chang, L. Wang, J. Zhang, Z. Zhou, C. Li, B. Chen, L. Etgar, G. Cui and S. Pang, *J. Mater. Chem. A*, 2017, **5**, 4803–4808.
25 Z. Zhou, Z. Wang, Y. Zhou, S. Pang, D. Wang, H. Xu, Z. Liu, N. P. Padture and G. Cui, *Angew. Chem., Int. Ed.*, 2015, **54**, 9705–9709.
26 B. Ding, Y. Ding, J. Peng, J. Romano-deGea, L. E. K. Frederiksen, H. Kanda, O. A. Syzgantseva, M. A. Syzgantseva, J.-N. Audinot, J. Bour, S. Zhang, T. Wirtz, Z. Fei, P. Dörflinger, N. Shibayama, Y. Niu, S. Hu, S. Zhang, F. F. Tirani, Y. Liu, G.-J. Yang, K. Brooks, L. Hu, S. Kinge, V. Dyakonov, X. Zhang, S. Dai, P. J. Dyson and M. K. Nazeeruddin, *Nature*, 2024, **628**, 299–305.
27 Y. Deng, C. H. Van Brackle, X. Dai, J. Zhao, B. Chen and J. Huang, *Sci. Adv.*, 2020, **5**, eaax7537.
28 J. Li, J. Dagar, O. Shargaieva, O. Maus, M. Remec, Q. Emery, M. Khenkin, C. Ulbrich, F. Akhundova, J. A. Márquez, T. Unold, M. Fenske, C. Schultz, B. Stegemann, A. Al-Ashouri, S. Albrecht, A. T. Esteves, L. Korte, H. Köbler, A. Abate, D. M. Többens, I. Zizak, E. J. W. List-Kratochvil, R. Schlatmann and E. Unger, *Adv. Energy Mater.*, 2023, **13**, 2203898.
29 R. Zhao, L. Tan, X. Luo, J. He, R. Dai, C. Feng, Q. Zhang, J. Yang and Y. Chen, *Angew. Chem., Int. Ed.*, 2024, **63**, e202319100.
30 M.-J. Zhang, N. Wang, S.-P. Pang, Q. Lv, C.-S. Huang, Z.-M. Zhou and F.-X. Ji, *ACS Appl. Mater. Interfaces*, 2016, **8**, 31413–31418.
31 D.-A. Le, K. Kala, T.-S. Su, N. Perumbalathodi and T.-C. Wei, *Sol. RRL*, 2024, **8**, 2400553.
32 T. Zhao, S. T. Williams, C.-C. Chueh, D. W. deQuilettes, P.-W. Liang, D. S. Ginger and A. K. Y. Jen, *RSC Adv.*, 2016, **6**, 27475–27484.
33 H. Fan, J.-H. Huang, L. Chen, Y. Zhang, Y. Wang, C. Gao, P. Wang, X. Zhou, K.-J. Jiang and Y. Song, *J. Mater. Chem. A*, 2021, **9**, 7625–7630.
34 J.-a. Yang, T. Qin, L. Xie, K. Liao, T. Li and F. Hao, *J. Mater. Chem. C*, 2019, **7**, 10724–10742.
35 Y. Jiang, E. J. Juarez-Perez, Q. Ge, S. Wang, M. R. Leyden, L. K. Ono, S. R. Raga, J. Hu and Y. Qi, *Mater. Horiz.*, 2016, **3**, 548–555.

36 Z. Xu, N. Liu, X. Liu, W. Han, W. Xu, J. Zhang, L. Huang, Z. Hu and Y. Zhu, *Chem. Eng. J.*, 2023, **451**, 139047.
37 G. I. Gurina and K. V. Savchenko, *J. Photochem. Photobiol., A*, 1995, **86**, 81–84.
38 R. A. Kerner, T. H. Schloemer, P. Schulz, J. J. Berry, J. Schwartz, A. Sellinger and B. P. Rand, *J. Mater. Chem. C*, 2019, **7**, 5251–5259.
39 D. Bogachuk, L. Wagner, S. Mastroianni, M. Daub, H. Hillebrecht and A. Hinsch, *J. Mater. Chem. A*, 2020, **8**, 9788–9796.
40 L. Gao, X. Li, Y. Liu, J. Fang, S. Huang, I. Spanopoulos, X. Li, Y. Wang, L. Chen, G. Yang and M. G. Kanatzidis, *ACS Appl. Mater. Interfaces*, 2020, **12**, 43885–43891.
41 O. I. Siidra, D. Y. Zenko, A. N. Suknotova and S. V. Krivovichev, *Mineral. Mag.*, 2013, **77**, 3239–3248.
42 P. Boher, P. Garnier, J. R. Gavarri and A. W. Hewat, *J. Solid State Chem.*, 1985, **57**, 343–350.
43 R. W. G. Wyckoff, *Crystal Structures*, Interscience Publishers, New York, 2nd edn, 1963.
44 R. Guo, B. Dahal, A. Thapa, Y. R. Poudel, Y. Liu and W. Li, *Nanoscale Adv.*, 2021, **3**, 2056–2064.
45 M. Bruggeman, M. Zelzer, H. Dong and A. Stamboulis, *Surf. Interface Anal.*, 2022, **54**, 986–1007.
46 A. Babayigit, D. Duy Thanh, A. Ethirajan, J. Manca, M. Muller, H.-G. Boyen and B. Conings, *Sci. Rep.*, 2016, **6**, 18721.
47 N. Ahn, K. Kwak, M. S. Jang, H. Yoon, B. Y. Lee, J.-K. Lee, P. V. Pikhitsa, J. Byun and M. Choi, *Nat. Commun.*, 2016, **7**, 13422.
48 T.-S. Su, T.-E. Fan, H.-K. Si, D.-A. Le, N. Perumbalathodi and T.-C. Wei, *Sol. RRL*, 2021, **5**, 2100109.
49 X. Zhang, J. Ye, L. Zhu, H. Zheng, G. Liu, X. Liu, B. Duan, X. Pan and S. Dai, *Nanoscale*, 2017, **9**, 4691–4699.
50 Z. Yang, X. Cao, G. Niu, Y. Wang, Y. Dong, S. Cao, W. Liu, X. Wang, Y. Liu and J. Wang, *Chem. Eng. J.*, 2023, **464**, 142720.
51 M. Long, T. Zhang, H. Zhu, G. Li, F. Wang, W. Guo, Y. Chai, W. Chen, Q. Li, K. S. Wong, J. Xu and K. Yan, *Nano Energy*, 2017, **33**, 485–496.
52 M. Fu, X. Shan, S. Wang, X. Zhao, R. Tao, L. You, Z. Deng, X. Fang and G. Meng, *ACS Appl. Electron. Mater.*, 2024, **6**, 4876–4882.
53 Z.-w. Kwang, C.-W. Chang, T.-Y. Hsieh, T.-C. Wei and S.-Y. Lu, *Electrochim. Acta*, 2018, **266**, 118–129.
54 T.-W. Ng, C.-Y. Chan, M.-F. Lo, Z. Q. Guan and C.-S. Lee, *J. Mater. Chem. A*, 2015, **3**, 9081–9085.
55 J. Chen, J. Lv, X. Liu, J. Lin and X. Chen, *Phys. Chem. Chem. Phys.*, 2023, **25**, 7574–7588.
56 F. Zeng, L. Xu, J. Xing, Y. Wu, Y. Zhang, H. Zhang, C. Hu, B. Dong, X. Bai and H. Song, *Advanced Science*, 2024, **11**, 2404444.